BMC Biology

RESEARCH

Open Access

Extracellular vesicles from adipose-derived mesenchymal stem cells alleviate acute lung injury via the CBL/AMPK signaling pathway

Yan Xiong[1†], Lulu Wang[1†], Bohao Li[1], Beibei Fu[1], Zhou Sha[1], Jin Liu[2], Rong Tian[3], Rui Yao[3], Feng Lin[1], Zixuan Cong[1], Yongliang Du[1], Xiaoyuan Lin[4*] and Haibo Wu[1*]

Abstract

Background Acute lung injury (ALI) which is caused by *Staphylococcus aureus* (SA), is a serious lung disease that threatens human health. Although some current treatments are effective in alleviating ALI, they still have a significant mortality rate. At present, adipose-derived mesenchymal stem cells (ADSCs)-derived extracellular vesicles (EVs) have been investigated for the treatment of various diseases. Here, we examined the role of ADSCs-derived EVs in regulating apoptosis and inflammation during ALI.

Results We showed that ADSCs and ADSCs-derived EVs supplementation could improve lung injury, restore mitochondrial function, and inhibit inflammation and apoptosis in ALI mice. Furthermore, miR-320a was present in EVs derived from ADSCs, and it can be transferred into lung tissue. *In vitro*, Casitas B-lineage lymphoma (CBL) expression was inhibited by miR-320a mimics. Finally, we found that miR-320a alleviated mitochondrial damage, inflammation, and apoptosis via the CBL/AMPK/JNK pathway.

Conclusions In conclusion, EVs from ADSCs could alleviate ALI via the CBL/AMPK signaling pathway. Therefore, the purpose of our study was to investigate the application of ADSC-derived EVs in mitigating ALI by modulating metabolic processes.

Keywords ALI, EVs, MiR-320a, AMPK, CBL, Energy metabolism

Background

SA is a gram-positive bacterium that can cause ALI. SA is widespread in the natural environment, including human and animal skin, air, and sewage [1]. In addition, SA causes a wide range of hospital-acquired and community-acquired infections commonly involving skin, bone, soft tissue, and lung infections [2]. Although antibiotics are effective in treating SA, methicillin-resistant SA and drug-resistant SA are still difficult global healthcare problems [3]. SA-induced ALI is a complex and deadly disease that seriously threatens human health. Severe inflammation is accompanied by excessive production of reactive oxygen species (ROS) in ALI [4]. Furthermore, uncontrolled ROS generation causes structural cellular damage, particularly to mitochondria [5, 6].

†Yan Xiong and Lulu Wang contributed equally to this work.

*Correspondence:
Xiaoyuan Lin
linxiaoyuan23@163.com
Haibo Wu
hbwu023@cqu.edu.cn
[1] School of Life Sciences, Chongqing University, Chongqing 401331, China
[2] School of Pharmaceutical Sciences, Chongqing University, Chongqing, China
[3] Department of Pathology, Chongqing Hygeia Hospital, Chongqing 401331, China
[4] Department of Clinical Microbiology and Immunology, College of Pharmacy and Medical Laboratory, Army Medical University (Third Military Medical University), Chongqing 400038, China

Damaged mitochondria result in epithelial cell apoptosis, alveolar damage, inflammatory cell aggregation, pulmonary edema, and increased lung permeability [7]. Current treatments for ALI include mechanical ventilation, restriction of fluid accumulation, application of antibiotics, and stem cell therapy. Although these treatments are effective in relieving ALI, recent data indicate that ALI still has substantial mortality [8]. However, the latest research indicates that mesenchymal stem cells (MSCs) therapy shows extremely promising applications in ALI [9]. Studies have demonstrated that MSCs have a positive function in ALI, and MSCs can not only promote regeneration and repair of damaged tissue but also regulate the immune process [10, 11].

MSCs have the ability to self-replicate and undergo multidirectional differentiation and can be isolated from adipose tissue, peripheral blood, bone marrow, and umbilical cord [12]. Furthermore, they can be induced to differentiate into adipocytes, chondrocytes, osteoblasts, and many other types of cells under specific conditions *in vitro* [13]. Thus, they are often considered ideal therapies for many medically intractable diseases. Recently, various studies have indicated that ADSCs play an important role in type 1 diabetes, skin repair, pain symptom relief, and immunomodulation [14–17]. In particular, ADSCs can enter damaged lung tissue and engraft as epithelial cells, endothelial cells, and fibroblasts to repair lung injury [18].

It has been demonstrated that EVs from ADSCs culture supernatant can reduce inflammation, decrease apoptosis, and promote the repair of pulmonary endothelial cells [19, 20]. EVs are small vesicles with a double membrane structure between 40–100 nm in diameter. The biogenesis of EVs involves double invagination of the plasma membrane and the formation of intracellular multivesicular bodies containing intraluminal vesicles [21]. It was indicated that EVs were released from various types of cells and were found in urine, saliva, blood, sperm, amniotic fluid, ascites, and breast milk. EVs contain a variety of biological components such as proteins, lipids, DNA, mRNAs, and non-coding RNAs [21, 22]. Following the fusion of EVs with the cell membrane, the contents will gain access to the cytoplasm of the target cells, subsequently impacting the associated signaling pathways [23, 24]. At present, miRNAs in EVs are becoming an increasingly popular field of research. miRNAs are a type of short non-coding RNAs that are usually between 20–24 nucleotides in length. Despite not encoding proteins, they are involved in the post-transcriptional control of gene expression. miRNAs suppress gene expression by targeting the 3'-untranslated region (3'-UTR) of specific mRNAs [25]. Moreover, miRNAs are involved in cell proliferation and differentiation, organismal metabolism, and host immunity [26].

It is widely acknowledged that ALI can lead to decreased mitochondrial function and energy metabolism in alveolar cells [27, 28]. Adenosine monophosphate-activated protein kinase (AMPK) is a crucial kinase that regulates energy homeostasis. AMPK is a fundamental molecule in biological energy metabolism and is responsible for maintaining the balance between cellular energy input and output, thus ensuring the correct functioning of cellular physiological activities. Once activated by decreasing energy status, AMPK promotes adenosine triphosphate (ATP) production, while shutting down the biosynthetic pathway to conserve ATP [29]. AMPK also regulates the expression of specific genes involved in energy metabolism to maintain body balance [30]. In addition, recent studies have revealed that AMPK can specifically regulate mitochondrial morphology, number, and function to maintain homeostasis [31]. Activated AMPK can not only affect metabolism by regulating mitochondrial homeostasis but also decrease the inflammatory response by inhibiting the activation of leukocytes, reducing the expression of adhesion molecules, and weakening the migration and adhesion of inflammatory cells [32]. Its position at the crossroads of energy metabolism makes AMPK an attractive therapeutic target in various diseases. Moreover, it has been demonstrated that activation of AMPK reduces lung inflammation in different disease models [33–35]. For this reason, AMPK is seen as a promising strategy for treating inflammatory lung diseases.

In this study, we found the impact of ADSCs EVs on SA-induced ALI. ADSCs-derived EVs attenuated lung injury through the reduction of mitochondrial damage and apoptosis. Subsequently, we discovered that miR-320a from EVs restored mitochondrial function and increased cellular activity by inhibiting CBL expression. In addition, CBL was shown to interact with AMPK and affect AMPK stability through ubiquitin modification. All these data suggest that ADSCs-derived EVs are a potentially effective treatment for ALI.

Results

ADSCs relieve SA-induced ALI

First, we investigated whether treatment with ADSCs relieved ALI in SA-infected mice. Mice were treated with ADSCs for 20 h after 4 h of infection (Additional file 1: Fig. S1A). A notable infiltration of inflammatory cells was found in the hematoxylin and eosin (H&E) staining after 24 h of infection. However, after intravenous injections of ADSCs, the histological lesions of the lungs were relieved compared with PBS and were accompanied with a decreased lung injury score (Additional file 1:

Fig. S1B-C). TNF-α is a central cytokine in inflammatory reactions. Therefore, we validated the inflammatory response in mice by examining TNF-α levels in different groups. In infected mice, SA significantly increased TNF-α levels in lung tissue, as measured by immunohistochemistry analysis (Additional file 1: Fig. S1D-E, Group 2). Notably, ADSC treatment markedly attenuated this phenomenon (Additional file 1: Fig. S1D-E, Group 4). The BALF protein concentration was further detected and we found that SA significantly increased the BALF protein concentration, while ADSCs decreased the BALF protein concentration (Additional file 1: Fig. S1F). Moreover, the BALF and lungs of ADSCs-treated mice infected with SA had lower bacterial loads than those of untreated mice (Additional file 1: Fig. S1G-H). The expression of inflammatory cytokines was also detected. As expected, interleukin-1beta (IL-1β), interleukin-6 (IL-6), monocyte chemoattractant protein-1 (MCP-1), and tumor necrosis factor-alpha (TNF-α) secretion were enhanced by SA and hampered by ADSCs. The results also revealed that ADSCs reversed SA-induced pulmonary inflammation (Additional file 1: Fig. S1I-L). To explore how ADSCs relieve ALI, we focused on changes in cellular energy metabolism. We analyzed OCR, which are indicative of mitochondrial function, through Seahorse XF Analyzers. The level of OCR was downregulated in SA-stimulated A549 cells, which was alleviated upon treatment with ADSCs (Fig. 1A). In addition, the levels of ATP and mitochondrial DNA (mtDNA) that were compromised by SA stimulation were markedly increased upon the application of ADSCs (Fig. 1B-C). Associated with this, Mito Tracker Red staining showed that ADSCs reduced the percentage of dysfunctional mitochondria (Fig. 1D-E). Mitochondrial membrane potential, as assessed by JC-1 staining, decreased under SA infection and increased following ADSC treatment (Fig. 1F-G). And the ROS level was also reduced with ADSC treatment (Fig. 1H-I). Mitochondrial fragmentation could result from enhanced fission or decreased fusion [36]. We thus analyzed whether SA infectin would affect total levels of key mitochondrial dynamics mediators, i.e., Mfn1, Mfn2, and Drp1. In Fig. 1J, the mRNA level of Drp1, a gene associated with mitochondrial fission, was increased, while the levels of Mfn1 and Mfn2, genes associated with mitochondrial fusion, were decreased following SA infection. However, ADSC treatment alleviated mitochondrial fragmentation. These data collectively indicate that SA infection induces abnormal energy metabolism in lung cells, which is alleviated by ADSCs. To date, no studies have specifically investigated the mechanisms by which ADSCs mitigate energy metabolism disturbances caused by SA infection. Therefore, this study aims to further elucidate these underlying mechanisms. To confirm the anti-apoptotic effect of ADSCs, we assessed the impact of treatment on the apoptotic capabilities of A5439 cells by cell counting kit-8 (CCK-8) and Caspase 3 activity assays (Fig. 1K-L). Moreover, ADSCs were discovered to significantly reduce Caspase 3 and BCL2 associated X (Bax) protein levels and enhance the expression of B cell leukemia/lymphoma 2 (Bcl-2) (Fig. 1M). Our data suggested that ADSCs played protective roles in SA-induced ALI.

ADSCs alleviate ALI via EVs

Previous studies have shown that EVs from ADSCs have therapeutic effects in a variety of diseases, including cancer, polycystic ovary syndrome, tubulointerstitial fibrosis, and bone regeneration [37–40]. To determine whether EVs from ADSCs play an important role in ALI, we pretreated ADSCs with GW4869, an inhibitor of EVs secretion (Fig. 2A). We can find that GW4869 did not affect the activity of ADSCs and secretion of other substances (IL-1β, IL-6, TNF-α) (Fig. 2B-C, Group 2). As expected, GW4869 significantly inhibited EVs secretion (Fig. 2D). Interestingly, pretreated GW4869-ADSCs did not relieve the histological lesions and damage situations in the lung tissues very well (Fig. 2E-F). IHC analysis of lung tissue sections from mice using an anti-TNF-α antibody revealed stronger brown staining in the GW4869-pretreated ADSCs group compared to the ADSCs group, indicating higher TNF-α expression in the GW4869-treated mice (Fig. 2G-H). In addition, GW4869-pretreated-ADSCs group had higher BALF protein concentrations than the ADSCs treatment group (Fig. 2I). Mice that received the GW4869-ADSCs

(See figure on next page.)

Fig. 1 ADSCs relieve SA-induced ALI *in vitro*. **A** Changes in cellular oxidative phosphorylation were detected by extracellular flux analysis. **B** and **C** ATP production and mtDNA expression in A549 cells. **D** Mito Tracker Red staining of mitochondria in A549 cells. Scale bar, 20 μm. Mito Tracker Red: red, DAPI: blue. **E** The quantitative analysis of mitochondrial fluorescence intensity. **F** The mitochondrial potential was observed via JC-1 staining. **G** The red to green fluorescence ratio was recorded to quantify the mitochondrial potential (rate). Scale bar, 20 μm. **H** ROS levels were assessed. **I** The relative fluorescence intensity ratio shown in (**H**) was analyzed. Scale bar, 20 μm. **J** qRT-PCR was performed to determine mRNA levels of mitochondrial fragmentation-related genes, including Drp1, Mfn1, and Mfn2. **K** Cell proliferation was determined by the CCK-8 assay. **L** Caspase 3 activity was measured in different groups. **M** The expression levels of Caspase 3, Bcl-2, and Bax were analyzed by Western blotting. Fluorescence images and blots were representative of six independent experiments. All data are presented as the mean ± SEM of $n = 6$. ***$p < 0.001$, **$p < 0.01$, *$p < 0.05$, ns, no significance

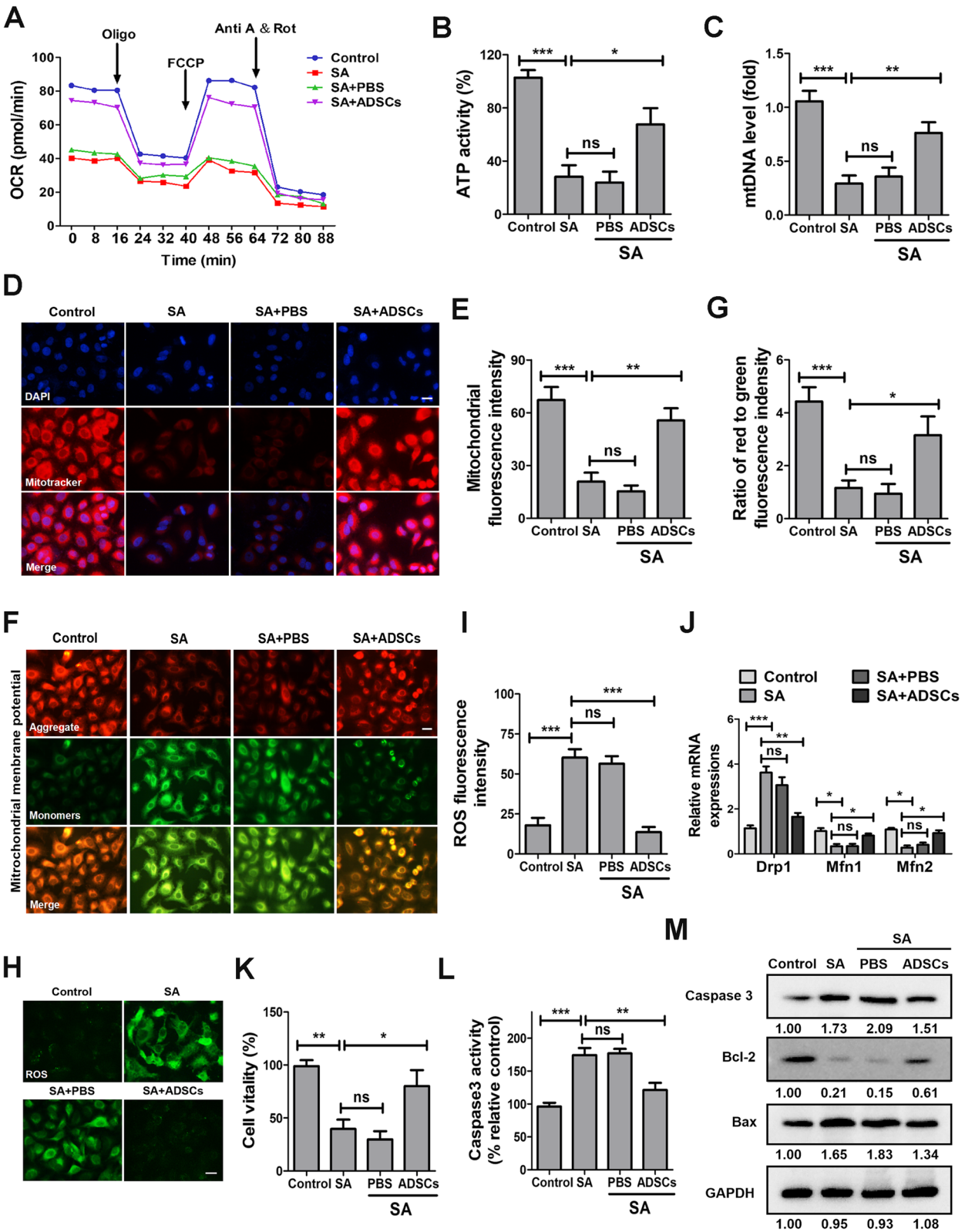

Fig. 1 (See legend on previous page.)

pretreatment did not show a significant reduction in bacterial loads in the lungs and BALF (Fig. 2J-K). Moreover, inhibition of EVs release with GW4869 did not dramatically delay the inflammatory response (Fig. 2L-O). Notably, pretreated GW4869-ADSCs played no therapeutic role, suggesting that targeting EVs secretion has therapeutic potential for ALI.

EVs released by ADSCs alleviate mitochondrial dysfunction and apoptosis

Next, to investigate whether ADSCs-derived EVs had a therapeutic effect on ALI, we isolated EVs from ADSCs and transmission electron microscopy (TEM) images showed that these EVs were usually spherical and had the characteristics of EVs (Fig. 3A). In our study, non-ADSC-derived EVs (293 T cell-derived EVs) were used as a negative control. As shown by nanoparticle analysis (NTA), the mean diameter of this particle was concentrated in the range of 50–100 nm (Fig. 3B). In addition, the typical EVs markers CD63 and CD9 were detected in the proteins extracted from EVs by Western blotting (Fig. 3C). Therefore, we confirmed that the isolated particles were indeed EVs (ADSC-derived EVs, non-ADSC-derived EVs). Then the therapeutic effects of EVs were demonstrated *in vitro*. The level of OCR was significantly improved after treatment with ADSC-EVs (Fig. 3D, Group 2). In addition, the levels of ATP and mtDNA were markedly increased upon the application of ADSC-EVs (Fig. 3E-F, Column 2). Relatedly, MitoTracker Red staining showed that mitochondrial damage was reduced by ADSC-EVs (Fig. 3G-H). Meanwhile, ADSC-EVs increased mitochondrial membrane potential (Fig. 3I-J), and decreased ROS release under SA infection (Fig. 3K-L). The mRNA level of Drp1 was decreased, while the levels of Mfn1 and Mfn2 were increased following ADSC-EVs treatment (Fig. 3M). Notably, we demonstrated that ADSCs-EVs also played an important role in alleviating apoptosis. This evidence can be obtained by CCK-8, Caspase 3 activity assays, and Western blotting analysis (Fig. 3N-P). Our results indicated that EVs released by ADSCs not only reduce lung injury and inflammation *in vivo* but also relieve mitochondrial damage and apoptosis *in vitro*. Interestingly, the inhibitor GW4869, by inhibiting the production and release of ADSC-derived EVs, significantly impaired the therapeutic efficacy of ADSCs in treating lung injury (Fig. 3D-P, Group 5). These findings suggest that the therapeutic effects of ADSCs are predominantly mediated through their EVs. Moreover, non-ADSC-EVs (293 T cell-derived EVs) failed to demonstrate comparable therapeutic effects (Fig. 3D-P, Group 6), further corroborating the unique role of mesenchymal stem cells in treatment and their functional dependence on specific EV-mediated mechanisms.

ADSCs-derived EVs relieve ALI via delivery of miR-320a

Currently, a significant number of miRNAs in EVs have demonstrated their importance in numerous diseases. In addition, we screened a number of prospective miRNAs based on the available literature [41]. To elucidate whether ADSCs-derived EVs miRNAs participate in the therapeutic process of ALI, we first compared the expression levels of different miRNAs in ADSCs-derived EVs. We noticed that the expression of miR-320a was the highest among the ten miRNAs determined in ADSCs-derived EVs (Fig. 4A). To demonstrate that highly expressed miR-320a was encapsulated in EVs. We used quantitative real-time PCR (qRT-PCR) to prove that RNase A treatment did not change the expression of miR-320a, while Triton X-100 combined with RNase A treatment substantially decreased the level of miR-320a (Fig. 4B). In addition, miR-320a expression was extremely elevated in EVs-treated lung tissues (Fig. 4C). To demonstrate the role of miR-320a, miR-320a knockout was performed using the CRISPR-Cas9 method based on ADSCs, and we isolated EVs from miR-320a KO-ADSCs for subsequent experiments. The knockout efficiency of miR-320a has been effectively validated (Additional file 1: Fig. S2A). TEM and NTA observations revealed that the knockout did not affect EV characteristics (Additional file 1: Fig. S2B-S2C). Similar results were obtained when EV markers were analyzed (Additional file 1: Fig. S2D). These findings suggest that miR-320a knockout has no impact on the quality of the EVs. Subsequently, an EV-based therapeutic model was established by intravenously administering EVs (WT-EVs and miR-320a KO-EVs) to mice (Fig. 4D). Interestingly, EVs deficient

(See figure on next page.)

Fig. 2 ADSCs alleviate ALI via EVs. **A** Timeline diagram of intranasal delivery and intravenous injection of ADSCs or pretreated GW4869-ADSCs. **B** Cell vitality was determined by the CCK-8 assay. **C** qRT-PCR was performed to measure the mRNA levels of IL-1β, IL-6, and TNF-α. **D** ADSCs were incubated with conditioned medium and conditioned medium with GW4869. Extract and detect EVs. **E** H&E staining of lung tissues. Scale bar, 400 μm. **F** The lung injury scores. **G** Immunostaining analysis of TNF-α expression in the lung tissues of mice. Scale bar, 100 μm. **H** Quantitative analysis of TNF-α-positive cells in the lung tissues. **I** The BALF protein concentration was determined by BCA ($n=6$). **J** and **K** SA bacterial loads in the BALF and lungs from mice treated with PBS, ADSCs, and ADSCs plus GW4869. **L**-**O** The expression of IL-1β, IL-6, MCP-1, and TNF-α in BALF was tested by ELISA. HE, IHC images and blots were representative of six independent experiments. All data are presented as the mean ± SEM of $n=6$. ***$p<0.001$, **$p<0.01$, *$p<0.05$, ns, no significance

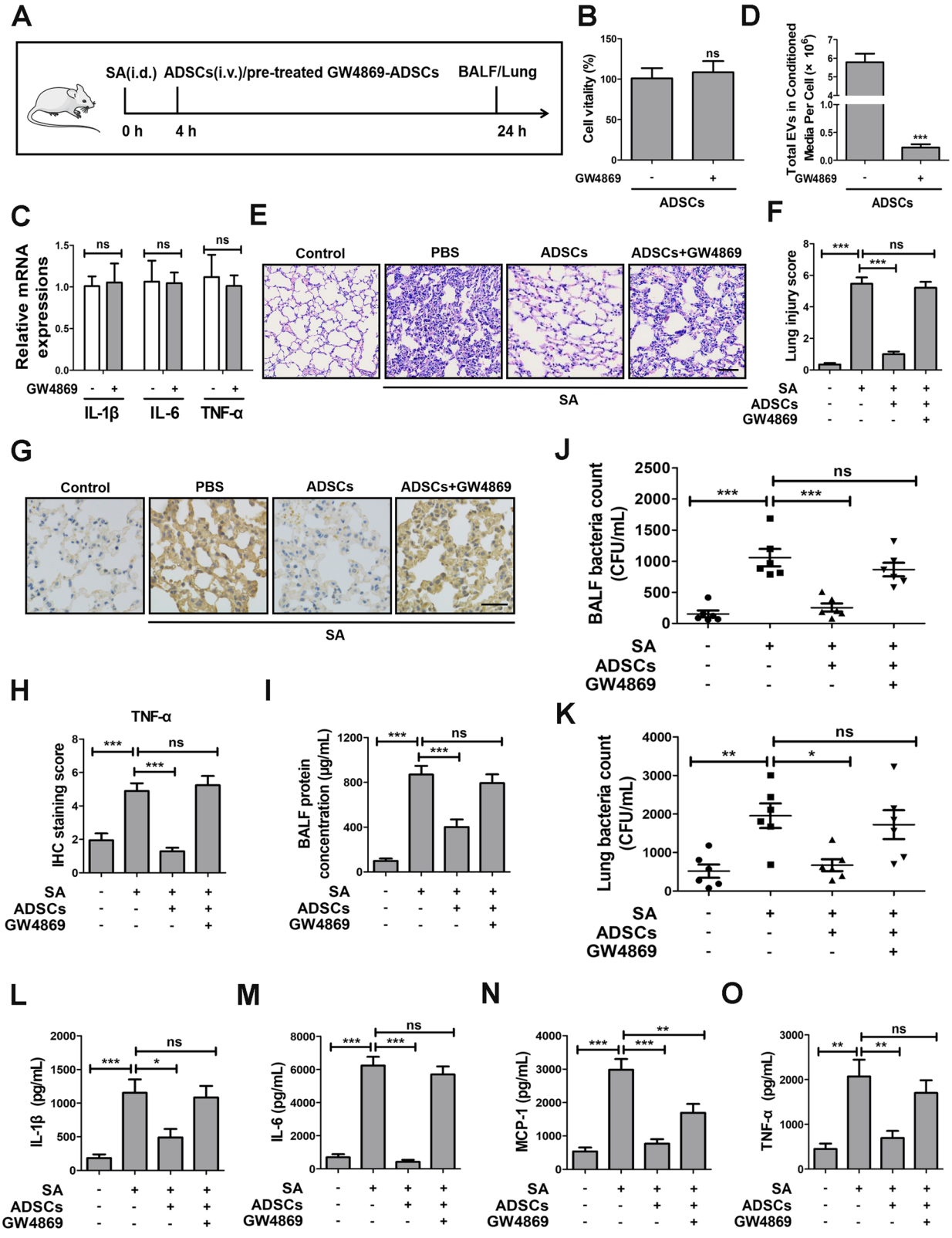

Fig. 2 (See legend on previous page.)

in miR-320a appeared to lose the ability to ameliorate ALI. The results indicated that miR-320a KO-EVs did not relieve the histological lesions and damage in the lung tissues very well (Fig. 4E-F). IHC analysis of lung tissue revealed higher TNF-α expression in miR-320a KO-EVs-treated mice (Fig. 4G-H). These results suggest that miR-320a plays a crucial role in the alleviation of lung injury through EVs. As shown in (Fig. 4I), the BALF protein levels in mice treated with miR-320a KO-EVs were significantly higher than those in the WT-EVs treatment group. Similarly, bacterial loads in the lungs and BALF were almost higher in the miR-320a KO-EVs treatment group (Fig. 4J-K). Moreover, only miR-320a enriched EVs had the ability to reduce the secretion of the inflammatory factors IL-1β, IL-6, MCP-1, and TNF-α and delay the inflammatory response (Fig. 4L-O). The analysis showed that EVs-derived miR-320a from ADSCs played a crucial role in mitigating lung injury.

miR-320a from EVs alleviates mitochondrial dysfunction and apoptosis

We used *in vitro* experiments to further demonstrate the role of miR-320a in mitochondrial damage. The level of OCR in A549 cells was significantly improved after transfection of the miR-320a mimic (Fig. 5A). Relatedly, the levels of ATP and mtDNA were markedly increased upon the application of the miR-320a mimic and decreased upon the application of the miR-320a inhibitor (Fig. 5B-C). In addition, mitochondrial damage was reduced by the miR-320a mimic, as shown by MitoTracker Red staining (Fig. 5D-E). miR-320a mimic increased mitochondrial membrane potential (Fig. 5F-G), and decreased ROS release under SA infection (Fig. 5H-I). The mRNA level of Drp1 was decreased, while the levels of Mfn1 and Mfn2 were increased following miR-320a mimic treatment (Fig. 5J). Meanwhile, we found that the miR-320a mimic also reduced apoptosis, as demonstrated by CCK-8 assays, Caspase-3 activity assays, and Western blotting analysis (Fig. 5K-M). Collectively, these results indicated that miR-320a could alleviate mitochondrial damage and restore energy metabolism in SA-infected ALI.

CBL is a direct target of miR-320a

AMPK regulates energy metabolic processes by modulating the morphology, number and function of mitochondria to maintain homeostasis [30]. Previous results have indicated that ADSCs-derived EVs can enhance energy metabolism in ALI (Figs. 2, 3), prompting further investigation into the regulation of AMPK in this process. We next investigated whether miR-320a targets and regulates specific genes during SA infection, thereby modulating AMPK activity. To acquire functional annotations and reference sequences, TargetScan.org was used to predict the targets of miR-320a. According to the prediction results, miR-320a targets six candidate E3 ligases (TRAF7, NEDD4L, MGRN1, SMURF2, RNF20, CBL) (Fig. 6A). In our study, we discovered that when CBL was inhibited by siRNA, protein levels of AMPK increased significantly (Fig. 6B). Therefore, these results reveal that no other E3 ligases are involved in this process, and CBL was selected for further study. CBL had a specific binding site for miR-320a in its 3'-UTR (Fig. 6C). Then we cotransfected miR-320a mimic and luciferase reporter constructs containing the WT or Mut-type UTR of CBL into HEK-293 T cells for dual-luciferase reporter (DLR) analysis. Our results showed that the miR-320a mimic dramatically inhibited the activity of the WT UTR of CBL, but not the Mut-type UTR (Fig. 6D). Moreover, we transfected miR-320a mimics into A549 cells and detected lower expression of CBL, while inhibition of miR-320a by the inhibitor significantly enhanced the level of CBL (Fig. 6E-F). In addition, both the miR-320a mimic and EVs significantly decreased the protein levels of CBL, as shown by the Western blotting results (Fig. 6G-H). Taken together, these data suggested that CBL was a direct target of miR-320a.

To evaluate the specificity of miR-320a targeting CBL, miR-320a was knocked out for functional validation. In our study, we built a co-culture model (Fig. 7A). In brief,

(See figure on next page.)

Fig. 3 EVs released by ADSCs alleviate mitochondrial dysfunction and apoptosis. **A** EVs from cells (ADSCs, 293 T cells) were extracted and identified by TEM. Scale bar, 100 nm. **B** EVs detection by NTA in FBS-free media. **C** Positively expressed EV markers CD63 and CD9 were detected by Western blotting. **D** Changes in cellular oxidative phosphorylation were detected by extracellular flux analysis. **E** The generation of ATP in different groups. **F** Assay of mtDNA expression in A549 cells. **G** Mito Tracker Red staining of mitochondria in different groups. Scale bar, 20 μm. Mito Tracker Red: red, DAPI: blue. **H** The quantitative analysis of mitochondrial fluorescence intensity. **I** The mitochondrial potential was observed via JC-1 staining. **J** The red to green fluorescence ratio was recorded to quantify the mitochondrial potential (rate). Scale bar, 20 μm. **K** ROS levels were assessed. **L** The relative fluorescence intensity ratio shown in (**K**) was analyzed. Scale bar, 20 μm. **M** qRT-PCR was performed to determine mRNA levels of mitochondrial fragmentation-related genes, including Drp1, Mfn1, and Mfn2. **N** Cell proliferation was determined by the CCK-8 assay. **O** Caspase 3 activity was measured in the control and EVs treated groups. **P** The expression levels of Caspase 3, Bcl-2, and Bax were analyzed by Western blotting. TEM, fluorescence images and blots were representative of six independent experiments. All data are presented as the mean ± SEM of $n = 6$. $^{***}p < 0.001$, $^{**}p < 0.01$, $^{*}p < 0.05$, ns, no significance

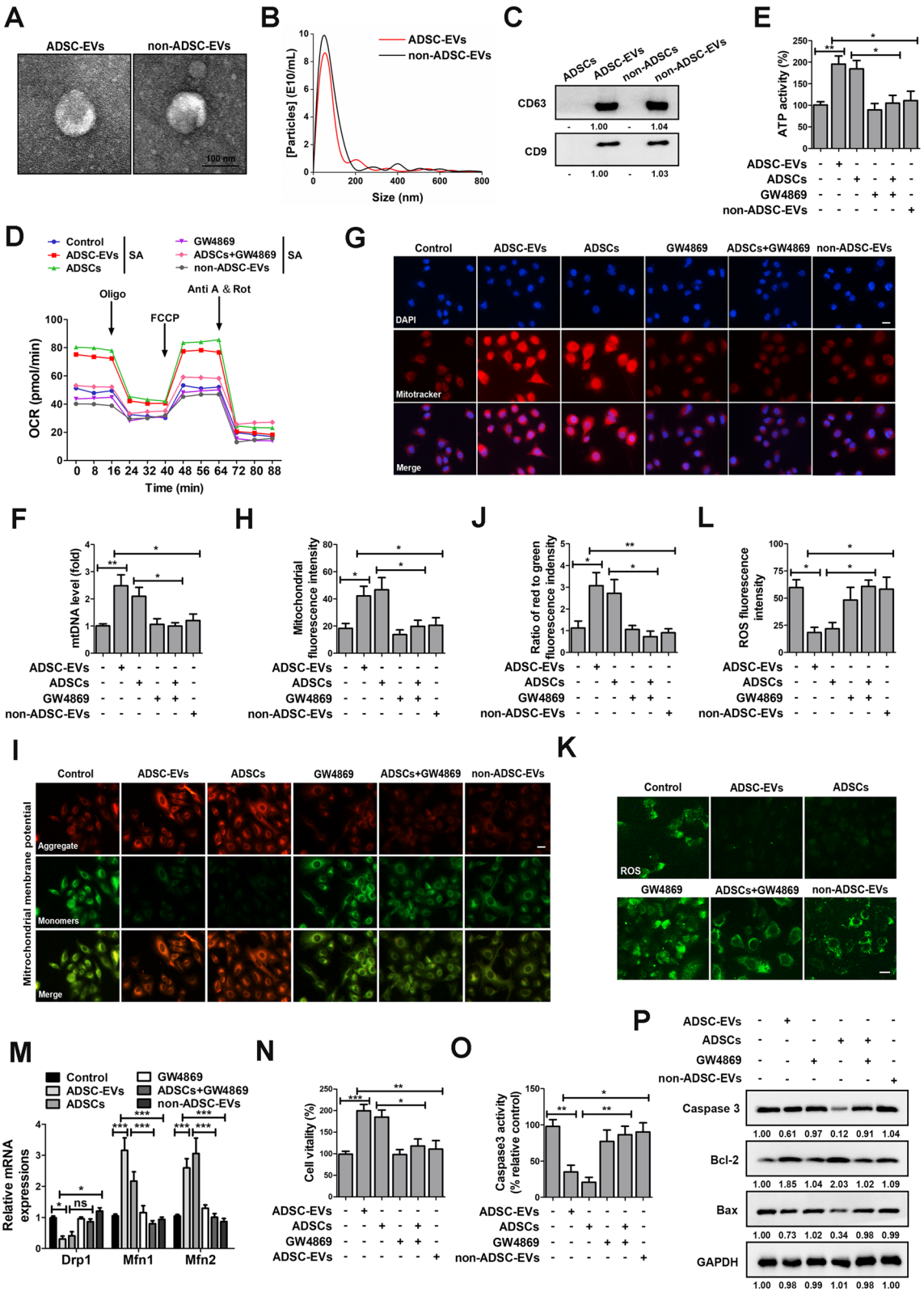

Fig. 3 (See legend on previous page.)

miR-320a was knocked out in ADSCs, and EVs were extracted from the cell culture medium using the previously described method (Fig. 4D). The miR-320a knockout efficiency was verified (Additional file 1: Fig. S2A). Subsequently, EVs were co-cultured with A549 cells (WT, si-CBL) for 24 h. The knockdown efficiency of CBL was validated (Fig. 7B). As shown in Fig. 7C, we found that the expression of miR-320a was increased in A549 cells following WT-EVs treatment (Column 2). This finding indicates that EVs can be delivered into A549 cells. Additionally, the expression of CBL was decreased by WT-EVs treatment (Fig. 7D-E, Column 2, Lane 2). There was no significant difference in the expression of miR-320a in A549 cells following miR-320a KO-EV treatment, and similar results were observed for CBL levels (Fig. 7D-E, Column 3, Lane 3). The level of OCR in A549 cells was significantly improved after treating WT-EVs (Fig. 7F). Relatedly, the levels of ATP and mtDNA were markedly increased upon the application of WT-EVs (Fig. 7G-H). In addition, mitochondrial damage was reduced by WT-EVs, as shown by MitoTracker Red staining (Fig. 7I-J). WT-EVs partially restored mitochondrial function, including an increase in mitochondrial membrane potential (Fig. 7K-L) and a decrease in ROS release under SA infection (Fig. 7M-N). The expression of Drp1 was decreased, while the expression of Mfn1 and Mfn2 was increased by WT-EV treatment (Fig. 7O). Notably, we demonstrated that WT-EVs also possess the capability to reduce apoptosis (Fig. 7P-R). The therapeutic effect of EVs was abolished upon miR-320a knockout (Fig. 7F-R, Group 3), whereas CBL knockdown resulted in a therapeutic effect similar to that of WT-EVs (Fig. 7F-R, Group 4). These results suggest that miR-320a specifically targets CBL and exerts its effects by inhibiting CBL.

miR-320a regulates the ubiquitination of AMPK by targeting CBL

Based on previous results, CBL was found to regulate AMPK (Fig. 6B). The mechanism underlying this regulation will be further explored. Firstly, AMPK expression showed an opposite trend to CBL under the miR-320a mimic treatment, and a decline in CBL was accompanied by an increase in AMPK expression (Fig. 8A). Furthermore, we found that MG132 (a proteasome inhibitor) could further enhance the level of AMPK (Fig. 8B). Therefore, we speculated that the E3 ligase CBL may have affected AMPK stability. The interaction between CBL and AMPK was tested by using coimmunoprecipitation (Co-IP). We confirmed that endogenous CBL interacted with AMPK in A549 cells (Fig. 8C). We also found an interaction between CBL and AMPK (Fig. 8D). To further explore the mechanism of CBL-mediated AMPK degradation, we conducted ubiquitination assays. When CBL was inhibited by siRNA, the ubiquitination of AMPK was reduced (Fig. 8E). As expected, inhibition of CBL by miR-320a mimics decreased the ubiquitination of AMPK (Fig. 8F). In Fig. 8G, we also confirmed that CBL promoted the formation of AMPK polyubiquitin chains (Fig. 8G). In the presence of Lys-48 and Lys-63 mutants, polyubiquitination of AMPK is not properly catalyzed by CBL (Fig. 8H). These observations suggested that CBL catalyzed AMPK to form Lys-48 and Lys-63 linked polyubiquitin chains, leading to the degradation of AMPK. Furthermore, the existing literature indicated that AMPK activation could inhibit the c-Jun N-terminal kinase (JNK) pathway and suppress the inflammatory response during hypoxia and reoxygenation [42]. We discovered that activated AMPK inhibited the phosphorylation of JNK (Fig. 8I). All these findings suggested that miR-320a alleviated ALI via the CBL/AMPK/JNK pathway.

Collectively, our results indicate that we discovered a novel therapeutic approach for regulating energy metabolism with ADSCs-derived EVs to alleviate ALI. miR-320a targets CBL and results in the activation of AMPK, thus leading to the inhibition of mitochondrial damage and cell apoptosis (Fig. 9).

Discussion

Reduced mitochondrial function in alveolar cells is known to occur in ALI. For example, mitochondrial dysfunction increased pulmonary microvascular hyperpermeability and disruption of mitochondrial bioenergetics induced endothelial barrier permeability [27, 28]. It has been demonstrated that enhanced mitochondrial biogenesis could rescue damaged type 2 pneumocytes and lung function in a mouse model of ALI [7]. Similarly,

(See figure on next page.)

Fig. 4 ADSCs-derived EVs relieve ALI via delivery of miR-320a. **A** The expressions of different miRNAs were analyzed by qRT-PCR in ADSCs-derived EVs. **B** qRT-PCR was used to determine EVs-derived miR-320a expression in the control, RNase A, and RNase A plus Triton X-100 groups. **C** miR-320a expression in mice lung tissues was detected by qRT-PCR. **D** Timeline diagram of intranasal delivery and intravenous injection of WT-EVs or miR-320a KO-EVs. **E** H&E staining of lung tissues. Scale bar, 400 μm. **F** The lung injury scores. **G** Immunostaining analysis of TNF-α expression in the lung tissues of mice. Scale bar, 100 μm. **H** Quantitative analysis of TNF-α-positive cells in the lung tissues. **I** BALF protein concentration was determined by BCA ($n=6$). **J** and **K** SA bacterial loads in BALF and lungs from mice treated with PBS, WT-EVs, and miR-320a KO-EVs. **L**-**O** The expression of IL-1β, IL-6, MCP-1, and TNF-α in BALF was tested by ELISA. HE, IHC images were representative of six independent experiments. All data are presented as the mean ± SEM of $n=6$. ***$p<0.001$, **$p<0.01$, *$p<0.05$, ns, no significance

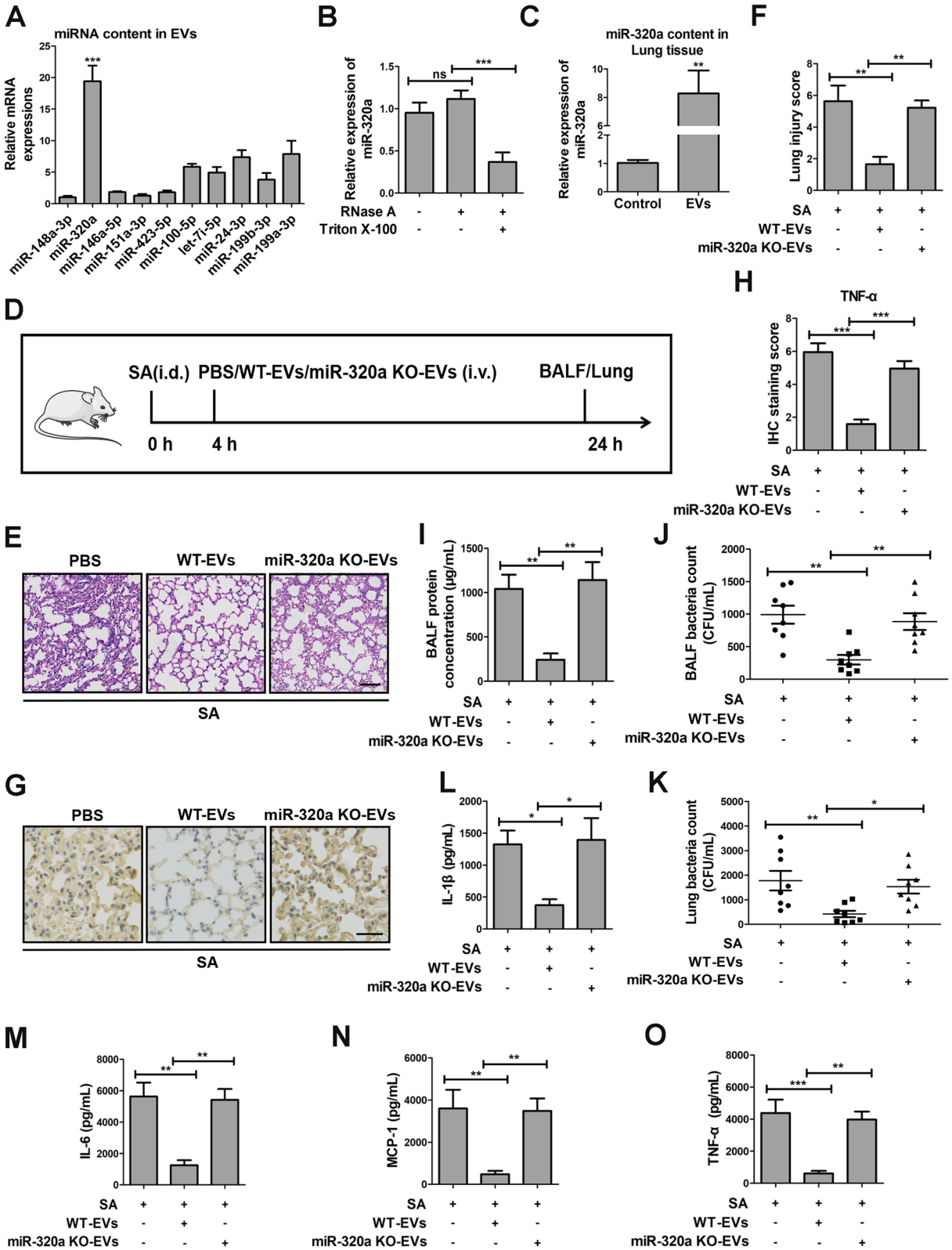

Fig. 4 (See legend on previous page.)

increased pulmonary ATP availability and turnover could also attenuate ALI in a rat model of acute pneumococcal pneumonia [43]. Therefore, alleviation of ALI through improvement of mitochondrial dysfunction is gradually being recognized as a valuable area of research. Previous studies have shown that MSCs have therapeutic effects in a variety of lung diseases, including ALI. For instance, miRNA-377-3p released from MSCs regulated autophagy and ameliorated lipopolysaccharide-induced ALI by targeting regulatory-associated proteins of mechanistic target of rapamycin [11]. Bone marrow mesenchymal stromal cells derived EVs alleviated sepsis-related ALI by inhibiting neutrophil extracellular trap formation [44]. miR-451 from MSCs-EVs reduced ALI by targeting the MIF-PI3K-AKT signaling pathway to modulate macrophage M2 polarization [45]. Notably, we focused on ADSCs-derived EVs to mitigate ALI by regulating mitochondrial homeostasis and energy metabolism. Our data are consistent with previous studies showing that MSCs are beneficial in the treatment of ALI. Interestingly, in our study, ADSCs were isolated from male mice for further investigation, with experimental methods based on established protocols [46]. Previous studies have reported that sex differences may influence the proliferation and differentiation capacities of ADSCs. For instance, ADSCs derived from female adipose tissue typically exhibit higher proliferative potential, whereas those from males may possess greater differentiation potential [47]. Despite these differences, current research suggests that sex itself does not significantly affect the therapeutic potential of ADSCs, particularly in *in vitro* experiments. This is because the therapeutic effects of ADSCs are primarily attributed to the secretion of cytokines and growth factors, which are more influenced by the cells' intrinsic states and culture conditions rather than direct effects of sex differences [48, 49]. Therefore, although this study did not account for sex as a variable, it remains appropriate for evaluating the therapeutic potential of ADSCs.

At present, miR-320 is associated with a wide range of disease processes. A recent study showed that EVs-derived miR-320a from MSCs suppressed hepatocellular carcinoma cell proliferation, migration, and metastasis by targeting pre-B-cell leukemia homeobox 3 [50]. Another study pointed out that miR-320a rescued mitochondrial ROS and cell death by regulating autophagy and lysosomal pathways in Parkinson's disease stress conditions [51]. Moreover, it has been reported that miR-320a could function as an anti-rheumatoid arthritis miRNA by suppressing CXC chemokine ligand 9 expression [52]. Our results showed that miR-320 from ADSCs-derived EVs alleviated SA-related ALI both *in vivo* and *in vitro*. We also observed that miR-320a targeted and inhibited CBL to upregulate AMPK-mediated metabolic pathways. In addition, we speculate that other miRNAs may also play a similar role and act synergistically with miR-320a in alleviating ALI. In Fig. 4A, the miRNAs significantly upregulated in the EVs include miR-100-5p, let-7i-5p, miR-24-3p, miR-199b-3p, and miR-199a-3p. Previous studies have demonstrated that certain miRNAs (let-7i-5p, miR-24-3p) can alleviate mitochondrial damage [53, 54], suggesting that these miRNAs may have potential therapeutic roles in the treatment of ALI. While our study focused on miRNA, especially miR-320a, we acknowledge that EVs contain a diverse array of bioactive molecules, including proteins, lipids, and other RNAs [55, 56], which may also contribute to their therapeutic effects. A more comprehensive characterization of EV contents will be a priority in future research.

In addition, as it is difficult to achieve better engraftment and differentiation efficacy of MSCs, more researchers have paid attention to MSCs-derived EVs. Surprisingly, MSC-EVs could retain the biological capabilities of MSCs and exhibit lower chances of stimulating tumorigenesis. This leads to a more dependable therapy with fewer adverse reactions [20]. Therefore, MSC-EVs could represent an innovative cell-free therapeutic approach. Currently, clinical trials explore miRNAs as therapeutics concentrate on tumors such as lung and liver cancers and other diseases. There exists a paucity of clinical trials investigating miRNAs for the diagnosis or treatment of ALI. However, more than 2000 miRNA genes have been identified in the human genome

(See figure on next page.)

Fig. 5 miR-320a from EVs alleviates mitochondrial dysfunction and apoptosis. **A** Changes in cellular oxidative phosphorylation were detected by extracellular flux analysis. **B** and **C** ATP production and mtDNA expression in A549 cells after transfection with miR-320a inhibitor and miR-320a mimics. **D** Mito Tracker Red staining of mitochondria in A549 cells. Scale bar, 20 μm. Mito Tracker Red: red, DAPI: blue. **E** The quantitative analysis of mitochondrial fluorescence intensity. **F** The mitochondrial potential was observed via JC-1 staining. **G** The red to green fluorescence ratio was recorded to quantify the mitochondrial potential (rate). Scale bar, 20 μm. **H** ROS levels were assessed. **I** The relative fluorescence intensity ratio shown in (**H**) was analyzed. Scale bar, 20 μm. **J** qRT-PCR was performed to determine mRNA levels of mitochondrial fragmentation-related genes, including Drp1, Mfn1, and Mfn2. **K** CCK-8 assay was used to determine the Cell proliferation. (L) Caspase 3 activity was measured in the control, miR-320a mimics, and miR-320a inhibitor groups. (M) The expressions of Caspase 3, Bcl-2, and Bax were analyzed by Western blotting. Fluorescence images and blots were representative of six independent experiments. All data are presented as the mean ± SEM of $n = 6$. ***$p < 0.001$, **$p < 0.01$, *$p < 0.05$, ns, no significance

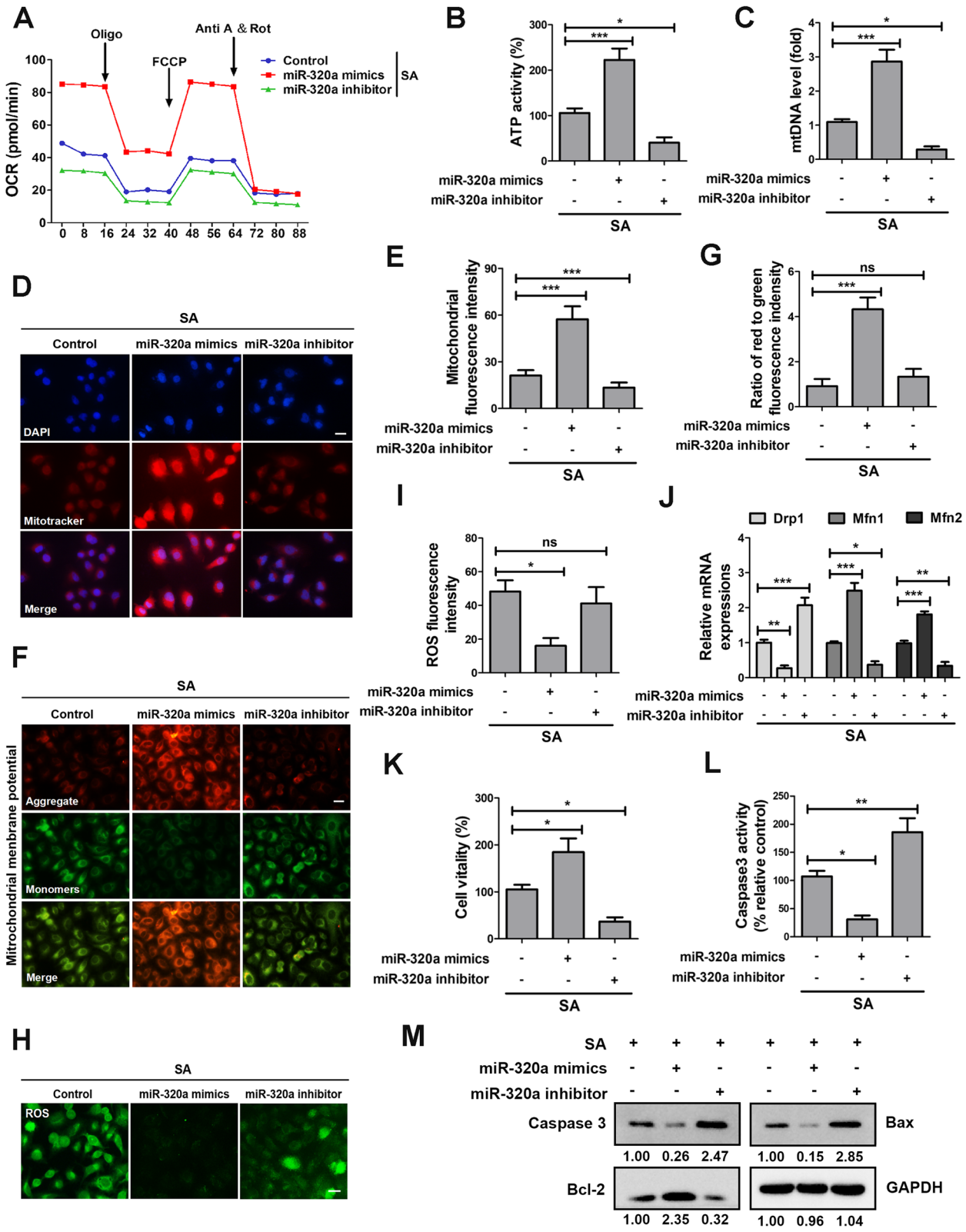

Fig. 5 (See legend on previous page.)

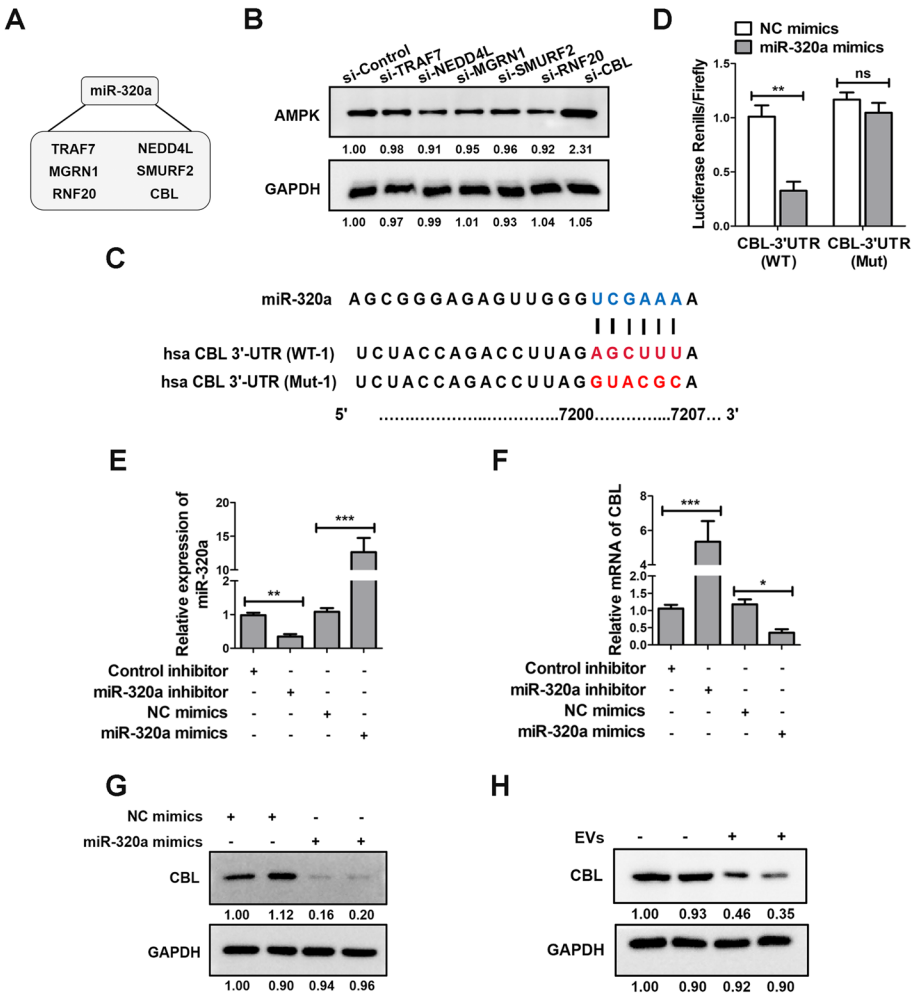

Fig. 6 CBL is a direct target of miR-320a. **A** The candidate E3 ligase targeted by miR-320a. **B** siRNA was transfected into A549 cells. The expressions of AMPK was analysed by Western blotting. **C** Predicted binding site of miR-320a and CBL 3′-UTR. **D** Luciferase activities in HEK-293 T cells cotransfected with miR-320a mimic and luciferase reporter constructs containing WT or Mut-type UTR of CBL. **E** A549 cells were transfected with control inhibitor, miR-320a inhibitor, NC mimics, and miR-320a mimics, the expression of miR-320a was detected by qRT-PCR. **F** qRT-PCR was used to detect the mRNA levels of CBL after transfection with the control inhibitor, miR-320a inhibitor, NC mimics, and miR-320a mimics. **G**-**H** A549 cells were treated with miR-320a mimic and EVs, and then cells were collected for Western blotting to show CBL expression. Blots were representative of six independent experiments. All data are presented as the mean ± SEM of $n = 6$. ***$p < 0.001$, **$p < 0.01$, *$p < 0.05$, ns, no significance

(See figure on next page.)

Fig. 7 The specificity of miR-320a targeting CBL. **A** A schematic diagram of the cellular model. **B** si-CBL was transfected into A549 cells. The expressions of CBL was analysed by Western blotting. **C** A549 cells were co-cultured with EVs (WT-EVs, miR-320a KO-EVs), and the expression of miR-320a was detected by qRT-PCR. **D** qRT-PCR was used to detect the mRNA levels of CBL after treatment with EVs (WT-EVs, miR-320a KO-EVs). **E** A549 cells were treated with EVs (WT-EVs, miR-320a KO-EVs), and then cells were collected for Western blotting to show CBL expression. **F** Changes in cellular oxidative phosphorylation were detected by extracellular flux analysis. **G** and **H** ATP production and mtDNA expression in A549 cells after treatment with EVs (WT-EVs, miR-320a KO-EVs). **I** Mito Tracker Red staining of mitochondria in A549 cells. Scale bar, 20 μm. Mito Tracker Red: red, DAPI: blue. **J** The quantitative analysis of mitochondrial fluorescence intensity. **K** The mitochondrial potential was observed via JC-1 staining. **L** The red to green fluorescence ratio was recorded to quantify the mitochondrial potential (rate). Scale bar, 20 μm. **M** ROS levels were assessed. **N** The relative fluorescence intensity ratio shown in (M) was analyzed. Scale bar, 20 μm. **O** qRT-PCR was performed to determine mRNA levels of Drp1, Mfn1, and Mfn2. **P** CCK-8 assay was used to determine the Cell proliferation. **Q** Caspase 3 activity was measured in the control, miR-320a mimics, and miR-320a inhibitor groups. **R** The expressions of Caspase 3, Bcl-2, and Bax were analyzed by Western blotting. Fluorescence images and blots were representative of six independent experiments. All data are presented as the mean ± SEM of $n = 6$. ***$p < 0.001$, **$p < 0.01$, *$p < 0.05$, ns, no significance

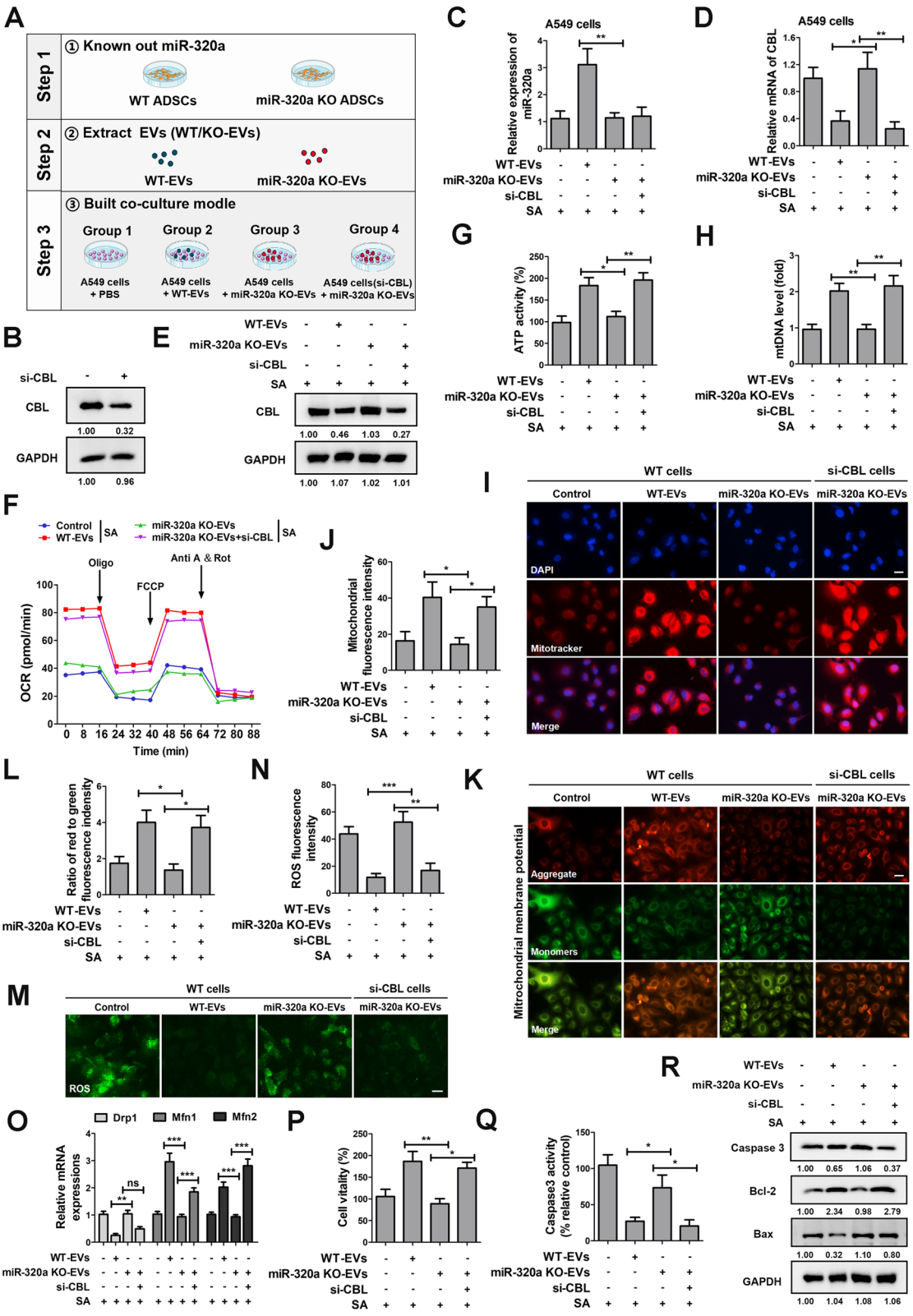

Fig. 7 (See legend on previous page.)

[57]. The increasing availability of human genome data inspires optimism that miRNAs can be used as diagnostic and treatment targets for ALI.

Conclusions

Our research presents miR-320a in MSCs-derived EVs that play a key role in regulating energy metabolism, inflammation, and apoptosis in ALI. Evidence from *in vivo* and *in vitro* experiments supports the benefits of ADSCs and ADSCs-derived EVs supplementation in improving lung injury, restoring mitochondrial function, and inhibiting inflammation and apoptosis. We further demonstrated the role of miR-320a in SA-induced ALI. The expression level of miR-320a in the lung showed a significant increase after the administration of EVs derived from ADSCs. This suggests that the EVs transferred miR-320a to the lung tissue. Furthermore, elevated miR-320a was found to inhibit CBL expression, which led to decreased ubiquitination of AMPK and increased AMPK accumulation. Finally, miR-320a alleviated mitochondrial damage, inflammation, and apoptosis via the CBL/AMPK/JNK pathway. Overall, our study expounded a theoretical basis for applying ADSCs-derived EVs to treat ALI.

Methods

ALI mice model

C57BL/6 male mice (body weight 20 ± 2 g) aged 8 weeks were purchased from Hunan SJA Laboratory Animal Co., Ltd. (Hunan, China) and raised in SPF with free access to food and water. The mice were intranasal delivery with around (2×10^8 CFU, 30 μL) SA (strain USA300) (or PBS as a control) for 4 h, and then the mice were given ADSCs (5×10^5) or EVs (10 μg/mL, 100 μL) by intravenous injection. After 20 h, the mice were euthanized by cervical dislocation. And bronchoalveolar lavage fluid (BALF) samples and lung tissues were collected for subsequent experiments. The total quantity of protein in BALF was measured using a bicinchoninic acid (BCA) protein assay kit provided by Beyotime Biotechnology. The lung tissues were collected for CFU assay or histopathology analysis.

Dislocation of the cervical vertebra

The murine tail is firmly grasped at its proximal segment with one hand, followed by positioning the animal on the cage grid. Simultaneous caudal traction and dorsal immobilization are achieved by securing the tail while applying forward pressure along the cervicothoracic axis using the middle and ring fingers, ensuring complete restraint. Press the mouse head down with the thumb and index finger of the other hand. Quickly pull the spinal cord and brain cord apart with force, and the mouse will generally die immediately. Postmortem protocols require prompt transfer of the specimen to a designated −20℃ cryopreservation unit for terminal storage.

Cell culture and treatment

ADSCs isolation and primary culture were performed as previously described [58]. Briefly, adipose tissue was collected from the inguinal of wildtype C57BL/6 mice (6-week-old, male, health). The adipose tissues were dispersed into small pieces and digested with 1 mg/mL collagenase I (Gibco, Darmstadt, Germany) at 37°C for 30 min. Then, an equal volume of DMEM/F12 medium (Gibco, Thermo Fisher Scientific, USA) containing 15% fetal bovine serum (FBS, Gibco, Thermo Fisher Scientific, USA) was added to the digested tissues. The cell suspensions were filtered and then centrifuged at 1,000 rpm for 5 min. Removed the supernatant and ADSCs were cultured with DMEM/F12.

A549 and HEK-293 T cells were obtained from the American Type Culture Collection (ATCC, Manassas, VA). The medium used in the experiment was composed of Dulbecco's modified Eagle's medium (DMEM, Gibco, USA), along with 10% FBS. All cells were kept in a humidified incubator at 37°C with CO_2.

A549 cells were infected with SA at a MOI of 10 for 12 h.

Plasmid construction and cell transfection

CBL (NM_005188.4) and AMPK (NM_001355035.2) coding sequences were inserted into the pCMV-Flag and pCMV-Myc vectors, respectively, as indicated. Primers consist of the following:

(See figure on next page.)

Fig. 8 miR-320a regulates the ubiquitination of AMPK by targeting CBL. **A** A549 cells were treated with the NC mimic and miR-320a mimic, and then cells were collected for Western blotting to show the expressions of CBL and AMPK. **B** A549 cells were treated with NC mimic or miR-320a mimic for 24 h, followed by MG132 treatment (20 μM) for 2 h. Expression of AMPK was assessed by Western blotting analysis. **C** The endogenous interaction of CBL and AMPK was tested in A549 cells. **D** Flag-CBL and Myc-AMPK plasmids were transfected into HEK-293 T cells, and CO-IP detected the interaction between CBL and AMPK. **E** Ubiquitination of AMPK was analyzed in WT and si-CBL A549 cells. **F** Ubiquitination of AMPK was analyzed in A549 cells transfected with NC mimics, and miR-320a mimics. **G** Flag-CBL, Myc-AMPK, and HA-ub plasmids were transfected alone or cotransfected into HEK-293 T cells, and the ubiquitination of AMPK was detected by CO-IP. **H** HEK-293 T cells were transfected with ubiquitin mutants (K48R and K63R), Myc-AMPK, and Flag-CBL. interaction between AMPK and ubiquitin was detected by Co-IP. **I** AMPK and p-JNK were detected by Western blotting. Blots were representative of six independent experiments

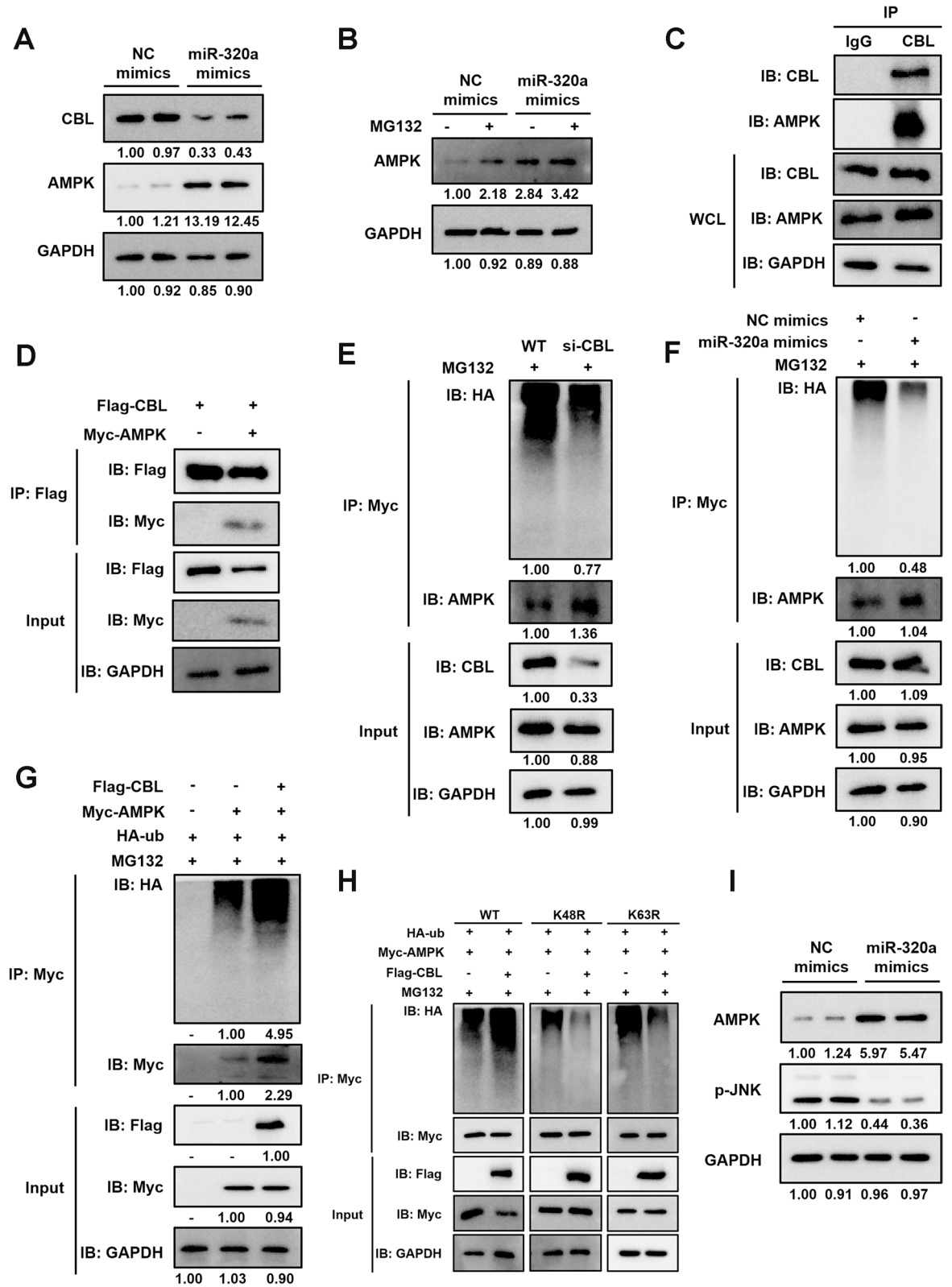

Fig. 8 (See legend on previous page.)

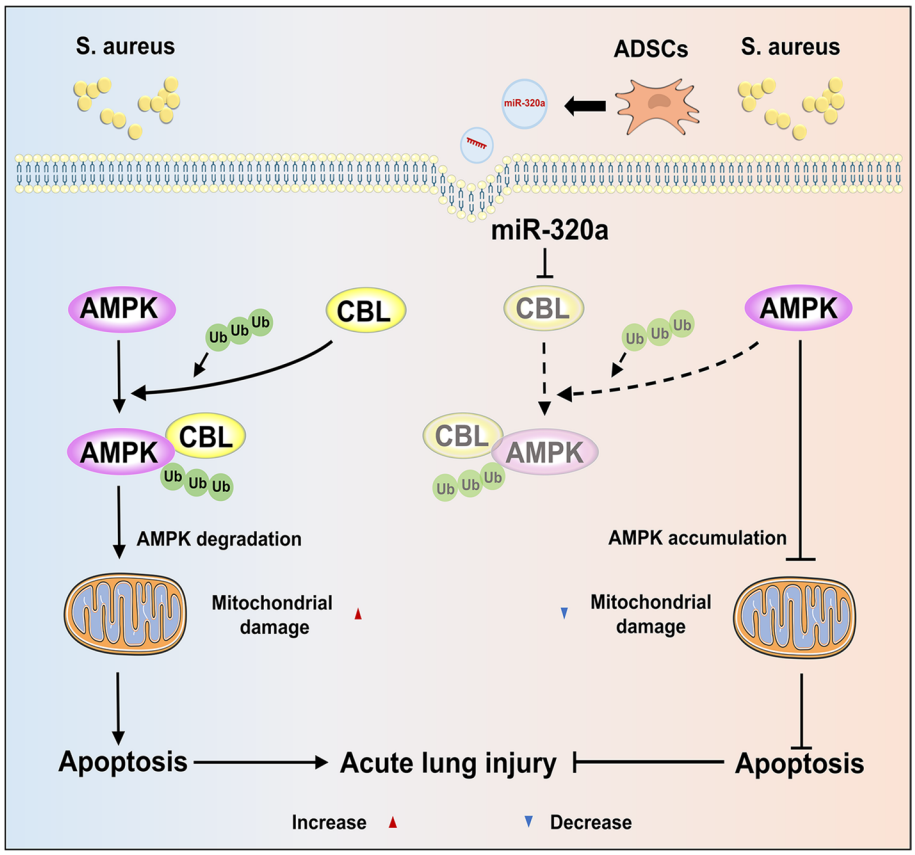

Fig. 9 miR-320a from ADSCs-derived EVs alleviates ALI. In the EVs-treated ALI mouse model, miR-320a decreased the ubiquitination of AMPK by inhibiting CBL expression. The accumulation of AMPK reduced the activation of the JNK pathway and alleviated mitochondrial damage, inflammation, and apoptosis

Flag-CBL, F- ATATGGATCCTCCTTGCAGCT GCTTAGACGCTG, R-TTAACTCGAGGGTAGCTACATGGGCAGG; Myc-AMPK, F-CCGGAATTC TTATGCTGCAGG TGGATCCCATGAAGA, R-CGGGGTACCTTA TTGTGCAAGAATTTTAATTAG.

A549 and HEK-293 T cells were transfected with mmu-miR-320a mimic (5'-AAAAGCUGGGUUGAG AGGGCGA-3'), mmu-miR-320a inhibitor (5'-UCG CCCUCUCAACCCAGCUUUU-3'), and their corresponding negative controls (GenePharma, China) by Lipofectermine 3000 (Thermo Fisher Scientific) for 48 h. siRNAs that target CBL were acquired from GenePharma (NCBI accession number: NM001284214.2) (Guangzhou, Guangdong, China). The Lipofectamine RNAiMAX reagent (Thermo Fisher Scientific) was used to transfect siRNAs according to the manufacturer's instructions. si-CBL for A549 cells: 5'- UCUUCUUCACGUUGCCGGCCA-3'.

Generation of CRISPR-Cas9-based knockout cells

miR-320a knockout (KO) cells were generated using the CRISPR-Cas9 method. sgRNAs (miR-320a KO-sgRNA: GGCAATACCCAGATACCTCA) were incorporated into the pSpCas9 (BB)−2A-Puro (PX459) plasmid after Bbs I digestion. The recombinant was then transfected into ADSCs by using Lipo 3000 Transfection Reagent (Invitrogen). After 48 h, puromycin (3 μg/mL) was used for the screening of individual colonies.

H&E staining and score

The lung tissue samples were fixed in 4% paraformaldehyde, paraffin embedded, and cut into 4 μm sections. H&E staining was carried out after deparaffinization of the slides. The lung injury score was calculated by a standard as follows: 0: no injury, 1: slight injury, 2: moderate injury, 3: serious injury, 4: very serious histological injury.

Immunohistochemistry

The lung tissues were segmented, fixed in 10% PFA, and embedded in paraffin. Sections were prepared at a thickness of 5 μm, followed by antigen retrieval. For IHC staining, the sections were incubated with a primary antibody against TNF-α (Beyotime, AF8208, 1:200), then with an HRP-conjugated secondary antibody (Beyotime, Jiangsu, China). The immunostaining signal was developed using 3,3-diaminobenzidine (DAB) substrate, and nuclei were counterstained with hematoxylin.

ELISA assay

The concentrations of IL-1β, IL-6, MCP-1, and TNF-α were analyzed in BALF of mice in each group through an ELISA kit (Thermo Fisher Scientific). The optical density was assessed by a microplate reader at 450 nm.

EVs extraction and identification

EVs derived from ADSCs cells were isolated by the EVs isolation kit (Umibio, Shanghai, China). The EVs were observed through a TEM and the markers CD63 and CD9 were confirmed through Western blotting analysis.

Luciferase reporter assay

The relative activity of CBL was determined by Dual-Luciferase reporter assay as previously described [59]. In brief, HEK-293 T cells were cotransfected with miR-320a or NC mimic and luciferase reporter constructs containing the WT or Mut-type UTR of CBL. After 24 h luciferase activities were measured by Dual-Luciferase reporter assay system (Promega).

Cell activity and apoptosis analysis

The CCK-8 Kit assay (Beyotime Biotechnology, China) and the Caspase 3 Activity Assay Kit (Biomol Research Laboratories, Plymouth Meeting, PA, USA) were used to test cell activity and apoptosis.

MitoTracker Red staining

A549 cells were seeded with 1×10^5 cells per well in twelve-well plates. According to the manufacturer's instructions, living cells were directly stained with MitoTracker Red probes (Beyotime, China). Fluorescence microscopy was employed to observe cells and the intensity of fluorescence was quantified by ImageJ.

JC-1 staining

Mitochondrial membrane potential was assessed using the JC-1 assay (Beyotime, C2006) according to the manufacturer's instructions. Cells were washed with PBS and incubated with the JC-1 probe for 30 min at 37°C in a 5% CO_2 environment, protected from light. Unbound dye was then removed with PBS, and fluorescence images were captured using a fluorescence microscope. Changes in mitochondrial membrane potential were quantified based on the red-to-green fluorescence ratio. For immunofluorescence analysis, the red and green fluorescence signals were converted to average grayscale intensities and analyzed using ImageJ software.

ROS production detection

Oxidative stress was measured using H_2DCFDA (D399, Invitrogen) following the manufacturer's protocol. Briefly, cells were incubated with 10 μM H_2DCFDA in culture medium at 37°C for 30 min. ROS levels were then evaluated by fluorescence microscopy.

ATP measurement

ATP was assayed using an ATP quantification bioluminescent kit (Beyotime Biotechnology, China) according to the manufacturer's instructions.

Extraction of mitochondrial DNA

According to the manufacturer's instructions, mitochondria were isolated using a Cell Mitochondria Isolation kit (Beyotime Biotechnology, China). And then use a FlexiGene DNA extraction kit (Qiagen, Germany) to extract the mitochondrial DNA.

Extracellular flux analysis

Oxygen consumption rates (OCR) was measured using an XFe96 Extracellular Flux Analyzer (Seahorse Bioscience, USA). Processed as follows: the ATP synthase inhibitor oligomycin (1 μM), the mitochondrial oxidative phosphorylation uncoupling agent FCCP (0.5 μM) to uncouple mitochondria, the mitochondrial complex I inhibitor rotenone (100 nM), and the mitochondrial complex III inhibitor antimycin A (1 μM). The basal OCR was determined by subtracting the OCR after exposure to rotenone and antimycin A from the OCR before oligomycin treatment. The maximal OCR was determined by subtracting the OCR after rotenone and antimycin A treatment from the OCR measured after the addition of FCCP.

Immunoblot and immunoprecipitation

Lung tissues, cells, and EVs were lysed in RIPA buffer. The protein concentration was determined by the BCA method. The primary antibodies used were as follows: Caspase 3 (NOVUS, NB100-56708, 1:1000), Bcl-2 (Beyotime, AF0060, 1:1000), Bax (Beyotime, AF0057, 1:1000), CBL (Santa Cruz, sc-1651, 1:1000), AMPK (CST, 83,506, 1:1000), Flag (Beyotime, AF0036, 1:1000), Myc (Beyotime, AF5054, 1:1000), HA (Beyotime, AF5057, 1:1000), and p-JNK (Beyotime, AJ516, 1:1000). Lysates were incubated overnight at 4°C with the appropriate antibodies

and Protein A/G beads (Thermo Fisher Scientific) for Co-IP, followed by immunoblotting.

Quantitative real-time PCR

RNAs from ADSCs-EVs and lung tissues by qRT-PCR experiments were performed using a SuperScript III One-Step RT-PCR kit (Thermo Fisher Scientific). The data were expressed using the $2^{-\Delta\Delta Ct}$ method. Primers are listed in Additional file 2: Table S1.

Statistical analysis

All statistical analyses were performed using GraphPad Prism 5 software. All data were derived from at least six independent experiments and were presented as mean ± standard error of the mean (SEM). The difference between the control and the experimental groups was analyzed using ANOVA and *t*-test. A p value of ≤ 0.05 was considered statistically significant.

Abbreviations

ALI	Acute lung injury
ADSCs	Adipose-derived mesenchymal stem cells
CBL	Casitas B-lineage lymphoma
MSCs	Mesenchymal stem cells
AMPK	Adenosine monophosphate-activated protein kinase
BALF	Bronchoalveolar lavage fluid
KO	Knockout
H&E	Hematoxylin and eosin
IL-6	Interleukin-6
TNF-α	Tumor necrosis factor-alpha
CCK-8	Cell counting kit-8
Bcl-2	B cell leukemia/lymphoma 2
NTA	Nanoparticle analysis
DLR	Dual-luciferase reporter
JNK	C-Jun N-terminal kinase
SA	Staphylococcus aureus
EVs	Extracellular vesicles
ROS	Reactive oxygen species
3′-UTR	3′-untranslated region
ATP	Adenosine triphosphate
BCA	Bicinchoninic acid
OCR	Oxygen consumption rates
IL-1β	Interleukin-1beta
MCP-1	Monocyte chemoattractant protein-1
mtDNA	Mitochondrial DNA
Bax	BCL2 associated X
TEM	Transmission electron microscopy
qRT-PCR	Quantitative real-time PCR
Co-IP	Coimmunoprecipitation

Supplementary Information

The online version contains supplementary material available at https://doi.org/10.1186/s12915-025-02178-y.

Additional file 1: Fig. S1. ADSCs relieve SA-induced ALI *in vivo*. Fig. S2. The characterization of miR-320a KO-EVs.

Additional file 2: Table S1. Primers used for qRT-PCR.

Additional file 3: Full-length, uncropped gel/blot images are presented.

Acknowledgements

Not applicable.

Authors' contributions

H.W., Y.X. and L.W. conceived and designed the study. B.L., B.F., Z.S., J.L., R.T., R.Y., F.L., Z.C., and Y.D. performed the experiments. H.W., Y.X. and L.W. analyzed the data. H.W., Y.X., L.W., and X.L. wrote the manuscript. All authors read and approved the final manuscript.

Funding

This work was supported by the National Natural Science Foundation of China (No. 92369115, 92469110, 82422048), the National Key Research and Development Program of China (No. 2024YFC2310800 and 2021YFC2301405), the Fundamental Research Funds for the Central Universities (No. 2024CDJXY-016), Natural Science Foundation of Chongqing, China (No. CSTB2023NSC-QMSX0402), and Chongqing Talents: Exceptional Young Talents Project (No. cstc2021ycjh-bgzxm0099). The funders had no role in study design, data collection and analysis, decision to publish, or preparation of the manuscript.

Data availability

All data generated or analyzed during this study are included in this published article and its supplementary information files (Additional files 1 and 2).

Declarations

Ethics approval and consent to participate

All animal experimental procedures complied with institutional regulations in accordance with the Animal Welfare Guidelines of Chongqing University.

Consent for publication

Not applicable.

Competing interests

The authors declare no competing interests.

Received: 11 September 2024 Accepted: 26 February 2025
Published online: 31 March 2025

References

1. Defres S, Marwick C, Nathwani D. MRSA as a cause of lung infection including airway infection, community-acquired pneumonia and hospital-acquired pneumonia. Eur Respir J. 2009;34(6):1470–6.
2. Tong SY, Davis JS, Eichenberger E, Holland TL, Fowler VG Jr. Staphylococcus aureus infections: epidemiology, pathophysiology, clinical manifestations, and management. Clin Microbiol Rev. 2015;28(3):603–61.
3. Hassoun A, Linden PK, Friedman B. Incidence, prevalence, and management of MRSA bacteremia across patient populations-a review of recent developments in MRSA management and treatment. Crit Care. 2017;21(1):211.
4. Galley HF. Oxidative stress and mitochondrial dysfunction in sepsis. Br J Anaesth. 2011;107(1):57–64.
5. Chang AL, Ulrich A, Suliman HB, Piantadosi CA. Redox regulation of mitophagy in the lung during murine Staphylococcus aureus sepsis. Free Radic Biol Med. 2015;78:179–89.
6. Zhang S, Zhao X, Xue Y, Wang X, Chen XL. Advances in nanomaterial-targeted treatment of acute lung injury after burns. J Nanobiotechnology. 2024;22(1):342.
7. Suliman HB, Kraft B, Bartz R, Chen L, Welty-Wolf KE, Piantadosi CA. Mitochondrial quality control in alveolar epithelial cells damaged by S. aureus pneumonia in mice. Am J Physiol Lung Cell Mol Physiol. 2017;313(4):699–09.
8. Hu Q, Zhang S, Yang Y, Yao JQ, Tang WF, Lyon CJ, et al. Extracellular vesicles in the pathogenesis and treatment of acute lung injury. Mil Med Res. 2022;9(1):61.
9. Dutra Silva J, Su Y, Calfee CS, Delucchi KL, Weiss D, McAuley DF, et al. Mesenchymal stromal cell extracellular vesicles rescue mitochondrial dysfunction and improve barrier integrity in clinically relevant models of ARDS. Eur Respir J. 2021;58(1):2002978.
10. Dos Santos CC, Amatullah H, Vaswani CM, Maron-Gutierrez T, Kim M, Mei SHJ, et al. Mesenchymal stromal (stem) cell therapy modulates

miR-193b-5p expression to attenuate sepsis-induced acute lung injury. Eur Respir J. 2022;59(1):2004216.
11. Wei X, Yi X, Lv H, Sui X, Lu P, Li L, et al. MicroRNA-377-3p released by mesenchymal stem cell exosomes ameliorates lipopolysaccharide-induced acute lung injury by targeting RPTOR to induce autophagy. Cell Death Dis. 2020;11(8):657.
12. Huss R. Isolation of primary and immortalized CD34-hematopoietic and mesenchymal stem cells from various sources. Stem Cells. 2000;18(1):1–9.
13. Rani S, Ryan AE, Griffin MD, Ritter T. Mesenchymal Stem Cell-derived Extracellular Vesicles: Toward Cell-free Therapeutic Applications. Mol Ther. 2015;23(5):812–23.
14. Kawada-Horitani E, Kita S, Okita T, Nakamura Y, Nishida H, Honma Y, et al. Human adipose-derived mesenchymal stem cells prevent type 1 diabetes induced by immune checkpoint blockade. Diabetologia. 2022;65(7):1185–97.
15. Silveira BM, Ribeiro TO, Freitas RS, Carreira ACO, Goncalves MS, Sogayar M, et al. Secretome from human adipose-derived mesenchymal stem cells promotes blood vessel formation and pericyte coverage in experimental skin repair. PLoS ONE. 2022;17(12):e0277863.
16. Amodeo G, Niada S, Moschetti G, Franchi S, Savadori P, Brini AT, et al. Secretome of human adipose-derived mesenchymal stem cell relieves pain and neuroinflammation independently of the route of administration in experimental osteoarthritis. Brain Behav Immun. 2021;94:29–40.
17. Bi Y, Lin X, Liang H, Yang D, Zhang X, Ke J, et al. Human Adipose Tissue-Derived Mesenchymal Stem Cells in Parkinson's Disease: Inhibition of T Helper 17 Cell Differentiation and Regulation of Immune Balance Towards a Regulatory T Cell Phenotype. Clin Interv Aging. 2020;15:1383–91.
18. Gupta N, Su X, Popov B, Lee JW, Serikov V, Matthay MA. Intrapulmonary delivery of bone marrow-derived mesenchymal stem cells improves survival and attenuates endotoxin-induced acute lung injury in mice. J Immunol. 2007;179(3):1855–63.
19. Khalaj K, Figueira RL, Antounians L, Lauriti G, Zani A. Systematic review of extracellular vesicle-based treatments for lung injury: are EVs a potential therapy for COVID-19? J Extracell Vesicles. 2020;9(1):1795365.
20. You J, Fu Z, Zou L. Mechanism and Potential of Extracellular Vesicles Derived From Mesenchymal Stem Cells for the Treatment of Infectious Diseases. Front Microbiol. 2021;12:761338.
21. Kalluri R, LeBleu VS. The biology, function, and biomedical applications of exosomes. Science. 2020;367(6478):eaau6977.
22. Isola AL, Chen S. Exosomes: The Messengers of Health and Disease. Curr Neuropharmacol. 2017;15(1):157–65.
23. Sun Z, Shi K, Yang S, Liu J, Zhou Q, Wang G, et al. Effect of exosomal miRNA on cancer biology and clinical applications. Mol Cancer. 2018;17(1):147.
24. Yang C, Zhang W, Baia M, Luo Q, Zheng Q, Yao Xu, et al. Edible plant-derived extracellular vesicles serve as promising therapeutic systems. Nano TransMed. 2023;100004:1–13.
25. Sinigaglia A, Peta E, Riccetti S, Venkateswaran S, Manganelli R, Barzon L. Tuberculosis-Associated MicroRNAs: From Pathogenesis to Disease Biomarkers. Cells. 2020;9(10):2160.
26. Duan W, Zhang W, Jia J, Lu Q, Eric GM. Exosomal microRNA in autoimmunity. Cell Mol Immunol. 2019;16(12):932–4.
27. Hough RF, Islam MN, Gusarova GA, Jin G, Das S, Bhattacharya J. Endothelial mitochondria determine rapid barrier failure in chemical lung injury. JCI Insight. 2019;4(3):e124329.
28. Lu Q, Zemskov EA, Sun X, Wang H, Yegambaram M, Wu X, et al. Activation of the mechanosensitive Ca(2+) channel TRPV4 induces endothelial barrier permeability via the disruption of mitochondrial bioenergetics. Redox Biol. 2021;38:101785.
29. Kahn BB, Alquier T, Carling D, Hardie DG. AMP-activated protein kinase: ancient energy gauge provides clues to modern understanding of metabolism. Cell Metab. 2005;1(1):15–25.
30. Viollet B, Foretz M, Guigas B, Horman S, Dentin R, Bertrand L, et al. Activation of AMP-activated protein kinase in the liver: a new strategy for the management of metabolic hepatic disorders. J Physiol. 2006;574(1):41–53.
31. Herzig S, Shaw RJ. AMPK: guardian of metabolism and mitochondrial homeostasis. Nat Rev Mol Cell Biol. 2018;19(2):121–35.
32. Park DW, Jiang S, Tadie JM, Stigler WS, Gao Y, Deshane J, et al. Activation of AMPK enhances neutrophil chemotaxis and bacterial killing. Mol Med. 2013;19(1):387–98.
33. Gregoire M, Uhel F, Lesouhaitier M, Gacouin A, Guirriec M, Mourcin F, et al. Impaired efferocytosis and neutrophil extracellular trap clearance by macrophages in ARDS. Eur Respir J. 2018;52(2):1702590.
34. Yuskaitis CJ, Jope RS. Glycogen synthase kinase-3 regulates microglial migration, inflammation, and inflammation-induced neurotoxicity. Cell Signal. 2009;21(2):264–73.
35. Hoogendijk AJ, Diks SH, van der Poll T, Peppelenbosch MP, Wieland CW. Kinase activity profiling of pneumococcal pneumonia. PLoS ONE. 2011;6(4):e18519.
36. Stavru F, Bouillaud F, Sartori A, Ricquier D, Cossart P. Listeria monocytogenes transiently alters mitochondrial dynamics during infection. Proc Natl Acad Sci U S A. 2011;108(9):3612–7.
37. Lou G, Chen L, Xia C, Wang W, Qi J, Li A, et al. MiR-199a-modified exosomes from adipose tissue-derived mesenchymal stem cells improve hepatocellular carcinoma chemosensitivity through mTOR pathway. J Exp Clin Cancer Res. 2020;39(1):4.
38. Cao M, Zhao Y, Chen T, Zhao Z, Zhang B, Yuan C, et al. Adipose mesenchymal stem cell-derived exosomal microRNAs ameliorate polycystic ovary syndrome by protecting against metabolic disturbances. Biomaterials. 2022;288:121739.
39. Chen L, Wang Y, Li S, Zuo B, Zhang X, Wang F, et al. Exosomes derived from GDNF-modified human adipose mesenchymal stem cells ameliorate peritubular capillary loss in tubulointerstitial fibrosis by activating the SIRT1/eNOS signaling pathway. Theranostics. 2020;10(20):9425–42.
40. Chen S, Tang Y, Liu Y, Zhang P, Lv L, Zhang X, et al. Exosomes derived from miR-375-overexpressing human adipose mesenchymal stem cells promote bone regeneration. Cell Prolif. 2019;52(5):e12669.
41. Xu F, Xiang Q, Huang J, Chen Q, Yu N, Long X, et al. Exosomal miR-423-5p mediates the proangiogenic activity of human adipose-derived stem cells by targeting Sufu. Stem Cell Res Ther. 2019;10(1):106.
42. Chen X, Li X, Zhang W, He J, Xu B, Lei B, et al. Activation of AMPK inhibits inflammatory response during hypoxia and reoxygenation through modulating JNK-mediated NF-kappaB pathway. Metabolism. 2018;83:256–70.
43. Beurskens CJ, Aslami H, Kuipers MT, Horn J, Vroom MB, van Kuilenburg AB, et al. Induced hypothermia is protective in a rat model of pneumococcal pneumonia associated with increased adenosine triphosphate availability and turnover*. Crit Care Med. 2012;40(3):919–26.
44. Zheng XL, Gu WJ, Zhang F, Zhao FZ, Li LZ, Huang HY, et al. Exosomal miR-127-5p from BMSCs alleviated sepsis-related acute lung injury by inhibiting neutrophil extracellular trap formation. Int Immunopharmacol. 2023;123:110759.
45. Liu J, Xing F, Fu Q, He B, Jia Z, Du J, et al. hUC-MSCs exosomal miR-451 alleviated acute lung injury by modulating macrophage M2 polarization via regulating MIF-PI3K-AKT signaling pathway. Environ Toxicol. 2022;37(12):2819–31.
46. Wu J, Yang Q, Wu S, Yuan R, Zhao X, Li Y, et al. Adipose-Derived Stem Cell Exosomes Promoted Hair Regeneration. Tissue Eng Regen Med. 2021;18(4):685–91.
47. Yasmeen R, Pham Q, Fukagawa NK, Wang TTY. Individual Variabilities in Adipose Stem Cell Proliferation, Gene Expression and Responses to Lipopolysaccharide Stimulation. Int J Mol Sci. 2022;23(20):12534.
48. Hutchings G, Janowicz K, Moncrieff L, Dompe C, Strauss E, Kocherova I, et al. The Proliferation and Differentiation of Adipose-Derived Stem Cells in Neovascularization and Angiogenesis. Int J Mol Sci. 2020;21(11):3790.
49. Foti R, Storti G, Palmesano M, Scioli MG, Fiorelli E, Terriaca S, et al. Senescence in Adipose-Derived Stem Cells: Biological Mechanisms and Therapeutic Challenges. Int J Mol Sci. 2024;25(15):8390.
50. Zhang Z, Li X, Sun W, Yue S, Yang J, Li J, et al. Loss of exosomal miR-320a from cancer-associated fibroblasts contributes to HCC proliferation and metastasis. Cancer Lett. 2017;397:33–42.
51. Shukla S, Currim F, Singh J, Goyani S, Saranga MV, Shinde A, et al. hsa-miR-320a mediated exosome release under PD stress conditions rescue mitochondrial ROS and cell death in the recipient neuronal and glial cells. Int J Biochem Cell Biol. 2023;162:106439.
52. Meng Q, Qiu B. Exosomal MicroRNA-320a Derived From Mesenchymal Stem Cells Regulates Rheumatoid Arthritis Fibroblast-Like Synoviocyte Activation by Suppressing CXCL9 Expression. Front Physiol. 2020;11:441.
53. Zhang H, Zou X, Liu F. Silencing TTTY15 mitigates hypoxia-induced mitochondrial energy metabolism dysfunction and cardiomyocytes apoptosis via TTTY15/let-7i-5p and TLR3/NF-kappaB pathways. Cell Signal. 2020;76:109779.

54. Zhou Y, Liu Y, Kang Z, Yao H, Song N, Wang M, et al. CircEPS15, as a sponge of MIR24-3p ameliorates neuronal damage in Parkinson disease through boosting PINK1-PRKN-mediated mitophagy. Autophagy. 2023;19(9):2520–37.
55. Dixson AC, Dawson TR, Di Vizio D, Weaver AM. Context-specific regulation of extracellular vesicle biogenesis and cargo selection. Nat Rev Mol Cell Biol. 2023;24(7):454–76.
56. Ferguson SW, Nguyen J. Exosomes as therapeutics: The implications of molecular composition and exosomal heterogeneity. J Control Release. 2016;228:179–90.
57. Lu Q, Yu S, Meng X, Shi M, Huang S, Li J, et al. MicroRNAs: Important Regulatory Molecules in Acute Lung Injury/Acute Respiratory Distress Syndrome. Int J Mol Sci. 2022;23(10):5545.
58. Kuang Y, Zheng X, Zhang L, Ai X, Venkataramani V, Kilic E, et al. Adipose-derived mesenchymal stem cells reduce autophagy in stroke mice by extracellular vesicle transfer of miR-25. J Extracell Vesicles. 2020;10(1):e12024.
59. Fu B, Lin X, Tan S, Zhang R, Xue W, Zhang H, et al. MiR-342 controls Mycobacterium tuberculosis susceptibility by modulating inflammation and cell death. EMBO Rep. 2021;22(9):e52252.

Publisher's Note